



Research paper

Effects of acetonitrile-assisted ball-milled aluminum nanoparticles on the ignition of acoustically levitated *exo*-tetrahydrodicyclopentadiene (JP-10) droplets



Stephen J. Brotton^a, Marc J. Malek^b, Scott L. Anderson^b, Ralf I. Kaiser^{a,*}

^a Department of Chemistry, University of Hawaii at Manoa, Honolulu, HI 96822, United States

^b University of Utah, Department of Chemistry, Salt Lake City, UT 84112, United States

HIGHLIGHTS

- Metal additives to improve performance of hydrocarbon fuels.
- Acoustic levitation of jet propellant droplets and carbon dioxide laser ignition.
- Ultraviolet-visible, Fourier-transform infrared, and Raman spectroscopies.
- Maximum flame temperature, combustion efficiency, and ignition delay time.
- Ignition mechanisms of aluminium (Al) nanoparticles.

ABSTRACT

We investigated the effects of aluminum nanoparticles produced by acetonitrile-assisted ball milling on the ignition of JP-10 droplets acoustically levitated in oxygen and argon. A carbon dioxide laser ignited the droplets, and the induced combustion processes were followed via ultraviolet-visible and Fourier-transform infrared spectroscopies together with a high-speed thermal-imaging camera. The increased ignition delay times, the reduced maximum flame temperatures, and the lower production of aluminum monoxide (AlO) radicals for the acetonitrile-milled aluminum sample suggest that its $\text{AlN}_n\text{C}_m\text{O}_v\text{H}_x$ surface layer limits oxidation of the aluminum core to a greater extent than the amorphous Al_2O_3 surface layer surrounding traditional aluminum nanoparticles.

1. Introduction

The hydrocarbon fuel tricyclo[5.2.1.0^{2,6}]decane (*exo*-tetrahydrodicyclopentadiene; $\text{C}_{10}\text{H}_{16}$; Scheme 1) or Jet Propulsion 10 (JP-10) has attractive properties for applications in air-breathing jet-propulsion missile systems including a high thermal stability, a low freezing point, and a high volumetric energy density of 39.6 kJ cm^{-3} [1–4]. JP-10 has consequently been extensively studied both experimentally and theoretically to understand its oxidation and thermal decomposition mechanisms [5]. Traditional hydrocarbon fuels such as JP-10 are limited, however, to a volumetric energy density of 40 kJ cm^{-3} . To improve the performance of air-breathing propulsion systems, methods to increase the energy density of the fuel are therefore required. The energy density of hydrocarbon fuels can be enhanced by adding high energy-density solids such as combustible metals; aluminum (Al), for example, with the high energy density of 84 kJ cm^{-3} [6] has generated considerable interest as a fuel additive [7–18]. The addition of Al particles to JP-10 has been shown to increase the

maximum flame temperatures, the burn times, and the combustion efficiencies in addition to reducing the ignition delay times [7–18].

Owing to the increased surface-area-to-volume ratio, the combustion rates of Al nanoparticles are higher than for micrometer-diameter aluminum particles [19–23]. Functionalizing the surface of Al nanoparticles with a variety of ligands such as alkenes has the advantage of improving their reactivity and dispersibility in fuels [24]. Wet chemistry methods based on organo-aluminum compounds have been employed to grow these ligand-capped Al nanoparticles [25–27]. However, for incorporation in fuels, the ligand-capped Al nanoparticles need to be produced inexpensively and in large quantities. One possible suitable fabrication approach capable of producing the larger quantities required and enabling the particle's surfaces to be functionalized involves high-energy milling in which the nanoparticles are abraded from the surfaces of aluminum balls [28]. To produce nanoparticles rather than only polishing the surfaces, the aluminum balls need to be milled together with a suitable liquid or vapor that binds strongly to the surfaces and diffuses rapidly into any cracks formed. The most suitable

* Corresponding author.

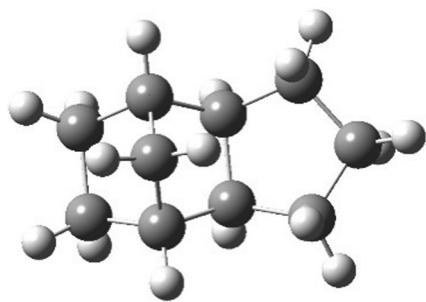
E-mail address: ralfk@hawaii.edu (R.I. Kaiser).

<https://doi.org/10.1016/j.cplett.2020.137679>

Received 20 May 2020; Received in revised form 30 May 2020; Accepted 1 June 2020

Available online 02 June 2020

0009-2614/ © 2020 Elsevier B.V. All rights reserved.



Scheme 1. Molecular structure of *exo*-tetrahydrodicyclopentadiene (JP-10). The carbon and hydrogen atoms are represented by the grey and white spheres, respectively.

milling agent was found to be acetonitrile (ACN) vapor, which produced aluminum particles with a mean diameter of approximately 35 nm. The resulting Al nanoparticles have flat, plate-like structures as a consequence of the milling.

These studies also employed density functional theory (DFT) to calculate the energetics for the binding of acetonitrile and the different dissociative fragments to the aluminum surface [28]. The undissociated acetonitrile molecule has a binding energy of only 25–42 kJ mol⁻¹ on an aluminum surface, and so should desorb from aluminum with a lifetime below 20 μs at room temperature. Therefore, acetonitrile must chemisorb to the surface by a mechanism in which acetonitrile first dissociates and the resulting fragments form stable bonds with the aluminum. The DFT calculations predict that the most energetically favorable pathway for the dissociative bonding of acetonitrile to aluminum involves cleavage of the C-C bond followed by attachment of the resulting CH₃ and CN fragments to the aluminum surface. The production of the Al nanoparticles consumes a factor of approximately 10 more acetonitrile than required to form the single, chemisorbed monolayer discussed above. During the milling, the chemisorbed acetonitrile decomposes to form mainly hydrogen (H₂) gas initially but also smaller quantities of methane (CH₄) and ethane (C₂H₆) in the later stages. The surface chemistry of the final nanoparticles produced was studied by X-ray photoelectron spectroscopy (XPS), which suggests that a layer of Al_nC_mH_x formed that oxidizes upon exposure to atmosphere to yield Al_nC_mO_vH_x with a thickness estimated to be 3.5 nm. A combination of thermogravimetric analysis and mass spectrometry (TGA-MS) were also used to investigate the composition of the surface layer. In descending order, the mole fractions desorbing from the samples were H₂ > CH₄ > C₂H₄ ≈ C₂H₆ > propene (C₃H₆) ≫ NH₃, which suggests that most of the nitrogen from the acetonitrile remained bonded to the aluminum nanoparticles. Thus, although the XPS spectrum in the Al 2p region cannot clearly distinguish between Al-O, Al-N, and Al-C bonds, these TGA-MS measurements favor the formation of strong nitride-like Al-N bonds.

Aluminum nanoparticles are traditionally manufactured by methods involving liquid-phase chemistry or vapor-phase condensation [21]. When exposed to air, aluminum forms an amorphous aluminum oxide (Al₂O₃) surface layer with a thickness of approximately 2–4 nm [23]. Several ignition mechanisms have been proposed for such standard nanoparticles, the details of which differ for nano- or micron-sized Al particles and different heating rates [20,21,23,29]. Broadly speaking, diffusion through the surrounding amorphous Al₂O₃ shell initially limits oxidation of the aluminum core. As the temperature increases, the amorphous Al₂O₃ undergoes a phase transformation into the crystalline cubic form γ-Al₂O₃. The aluminum core melts and expands, which exerts pressure on the brittle γ-Al₂O₃ layer and, hence, cracks form. The resulting increased exposure of the aluminum core to the oxidizer releases significant energy and thus causes the particle to ignite. The ignition mechanism probably differs for the Al_nC_mO_vH_x surface and flat, plate-like structures for the Al nanoparticles produced

by high-energy milling with acetonitrile.

We reported previously on the effects of untreated, prestressed, and superquenched aluminum particles with mean diameters of 100 nm, 250 nm, 500 nm, 1.6 μm, and 8.8 μm on the oxidation of JP-10 droplets acoustically levitated in an oxygen-argon mixture [30]. A carbon dioxide laser ignited the aluminum-containing JP-10 droplets, and the induced combustion processes were followed via ultraviolet-visible (UV-Vis), Fourier-transform infrared (FTIR), and Raman spectroscopies together with high-speed optical and IR thermal-imaging cameras. We found that the aluminum particles were necessary to ignite the JP-10 droplets and resulted in higher flame temperatures. The effects of the aluminum particles on the combustion processes increased for smaller diameters, although the different stress treatments did not cause observable variations. We thus demonstrated the suitability of the present levitator apparatus to study the ignition of hydrocarbon fuels with energy densities enhanced by metal additives.

To probe the acetonitrile-milled aluminum particles, X-ray photoelectron spectroscopy, thermogravimetric analysis combined with mass spectrometry, infrared spectroscopy, dynamic light scattering, scanning electron microscopy, and helium ion microscopy were employed [28]. However, the effects of the acetonitrile-milled aluminum particles with their different surface-layer composition and flat, plate-like shape on the ignition of hydrocarbon fuels has not been studied. We therefore used the levitator experimental apparatus to investigate the effects of the acetonitrile-milled aluminum nanoparticles on the ignition of JP-10 droplets and compared the results with those for standard 100 nm-diameter untreated aluminum particles surrounded by an amorphous Al₂O₃ layer. More specifically, for each type of aluminum nanoparticle dispersed in a JP-10 droplet, we measured and compared the temperature temporal profiles of the combustion process to obtain the ignition delay times and the maximum flame temperatures reached; we recorded the ultraviolet-visible (UV-Vis) emission spectra at the instant of ignition to identify the reactive intermediates, the individual atoms, and the molecules produced by the oxidation; and finally we measured the FTIR transmission spectrum of the gaseous products after the combustion to identify the final state molecules. The resulting information is used to provide insight into the suitability of acetonitrile-milled aluminum particles as a metal additive to hydrocarbon fuels such as JP-10.

2. Experimental methods

The analytes were prepared by mixing 1% by wt. of the ACN-milled or untreated aluminum nanoparticles with JP-10 and then homogenizing ultrasonically. The Al nanoparticles were dispersed uniformly throughout the droplet following sonication, and the experiments were completed before any significant separation occurred between the particles and the liquid. The particle size distributions were measured by dynamic light scattering (DLS), which gave a mean diameter and standard deviation of 34 ± 9 nm or 97 ± 9 nm for the ACN-milled or untreated particles, respectively. A droplet of JP-10 containing one of these aluminum nanoparticle types was levitated in an ultrasonic levitator. The levitator experimental apparatus has been reviewed in detail previously [31,32]. The levitator is enclosed within a pressure-compatible process chamber to enable the droplet to be studied in the gas or gases of interest. In the present experiments, the chamber was filled with a 60% oxygen and 40% argon gas mixture at a total pressure of 936 Torr. The droplets studied were oblate spheroids with horizontal and vertical diameters varying from 2.0 to 2.8 mm and 1.2 to 1.6 mm, respectively. A droplet was dispensed into the central pressure minimum using a microneedle attached to the end of a wobble stick, which enables full translational motion of the needle and rotation about its central axis. The needle is connected via chemically inert polyetheretherketone (PEEK) tubing and a then vacuum compatible valve to a syringe located on the outside port of the process chamber.

The droplets were ignited using a carbon dioxide laser emitting at a

wavelength of 10.6 μm with a power adjustable between 1 W and 40 W. The duty cycle of the laser was set to 80% for all experiments, which produced an output power of 32 W. To aid ignition the laser beam was focused to a small diameter ($1/e^2$) of 0.2 mm on the droplet, which was achieved using an 8X beam expander to minimize the limitation by diffraction followed by a copper parabolic mirror with a focal length of 300 mm. An optical model describing the propagation of the CO_2 laser beam through a JP-10 droplet containing Al particles has been developed in the [Supporting Information](#) of Ref. [30].

UV-Vis, FTIR, and Raman spectroscopies were employed to follow the oxidation processes during and after the ignition event. In the UV-Vis spectrometer set-up, a fiber-optic probe located inside of the process chamber is supported by an x, y, z manipulator, which permits the read fiber to be aligned on the droplet at a separation of approximately 6 mm. The UV-Vis spectrum emitted by the igniting droplet is collected by the read fiber, leaves the chamber by a conflat fiber-optic feed-through, and lastly is dispersed in a StellarNet SILVER-Nova UV-Vis spectrometer. The spectrometer covers the 200 nm to 1100 nm wavelength range and has a resolution of 2 nm. The gases produced within the process chamber were identified by FTIR transmission spectroscopy in the 400–4000 cm^{-1} wavenumber region by combining a Nicolet 6700 FTIR spectrometer (Thermo Scientific) with two stages of copper mirror optics. Raman spectra of the droplet were collected *in situ* using a Q-switched Nd:YAG laser operating at 532 nm. The Raman-shifted photons, backscattered from the droplet, were focused by a lens into a HoloSpec *f*/1.8 holographic imaging spectrograph equipped with a PI-Max 2 ICCD camera (Princeton Instruments). The spectra were collected over the two Raman-shift ranges of 300–2450 cm^{-1} and 2400–4400 cm^{-1} simultaneously. FTIR spectra of the JP-10 droplets containing the aluminum nanoparticles before levitation were recorded by an attenuated total reflection (ATR) accessory placed inside the FTIR spectrometer. High-speed optical videos of the igniting droplets were recorded with a Phantom Miro 3a10 camera at frame rates of up to 1000 per second.

Infrared thermal-imaging videos of the ignition event were recorded using an FLIR A6703sc camera. A delay of 0.2 s between the starting pulses sent first to the infrared camera and then to the CO_2 laser enabled precise synchronization of their respective timescales and for the temperature of the droplet to be recorded before the ignition. To operate at the higher frame rate of 387.55 s^{-1} a $1/4$ window was employed, which corresponds to 160×120 pixels and a $10 \text{ mm} \times 8 \text{ mm}$ field of view (FOV) centered on the droplet. Videos for separate ignition events were recorded over each temperature range of 283–363 K, 353–473 K, 423–623 K, 523–873 K, 773–1473 K, and 973–1773 K, where the quoted temperatures are the values before correcting for the emissivity. To improve the statistical accuracy for the highly stochastic combustion processes, five ignition events were recorded for each temperature range giving a total of 30 videos. The videos were converted to temporal plots of the maximum temperature within the $10 \text{ mm} \times 8 \text{ mm}$ FOV and subsequently combined to give a single-temperature temporal profile over the full range of observed temperatures.

The emissivity of luminous, sooty flames can be approximated by [33]

$$\epsilon = 1 - e^{-kl} \quad (1)$$

where k is the absorption coefficient and l is the effective path length in the flame. To our knowledge, the absorption coefficient k for flames produced by JP-10 containing Al nanoparticles has not been measured and determining the path length l precisely is not practicable. Therefore, placing the flame temperature obtained from the IR camera on an absolute scale via equation (1) would be highly inaccurate. Instead, we therefore simultaneously recorded an IR thermal video and measured a UV-Vis emission spectrum of the same ignition event. The absolute temperature of the ignition was determined by performing a black-body fit to the background of the UV-Vis spectrum (Section 3.2). The emissivity in the FLIR ResearchIR Max program was then set to the value

that gave the same flame temperature as obtained from the black-body fit. The resulting value for the emissivity of 0.115 was used to calibrate the flame temperatures for all subsequent measurements. The calibration with $\epsilon = 0.115$ was applied only at temperatures above the autoignition temperature of JP-10 corresponding to 509 K.

To produce the ACN-milled Al nanoparticles, 200 g of wash-milled aluminum balls with diameters of 9 mm were first placed in a 250 mL tungsten-carbide milling jar under a nitrogen atmosphere. The jar was purged and then pressurized to 4.1×10^4 Pa with argon before adding 5 mL of acetonitrile and milling in a Retsch PM 400 planetary ball mill for four hours at 350 rpm. Inside a nitrogen glovebox, approximately 10 g of Al powder was recovered from the products of the milling. Finally, the Al particles were oxidized and, hence, passivated by slowly exposing the powder to air within the glovebox. Scanning electron microscope images showing the sizes and shapes of the Al particles produced by milling in ACN vapor are presented in the [Supporting Information](#) of Yu et al [28]. The untreated Al particles with a mean diameter of 100 nm were purchased from Novacentrix.

3. Results and discussion

3.1. Temperature temporal profiles

The temperature temporal profiles for the ignition of a JP-10 droplet containing ACN-milled Al nanoparticles or untreated Al nanoparticles are compared in Fig. 1. The profiles for both types of nanoparticle display several stages in common. In the pre-ignition stage, the temperature rises to a value below the autoignition temperature of JP-10 corresponding to 509 K after approximately 4 ms of laser irradiation. In the second stage, ignition of the Al nanoparticles occurs by the following mechanism: the tightly focused laser beam first causes a plume of Al particles to be ejected from the surface of the JP-10 droplet and JP-10 to evaporate rapidly [30]. An ejected Al particle crossing the path of the carbon dioxide laser beam in the oxygen-argon mixture then ignites, which subsequently causes the nearby Al particles and JP-10 vapor to combust. During this Al ignition stage, the temperature rises rapidly at the maximum rates of $7.7 \times 10^5 \text{ K s}^{-1}$ and $9.5 \times 10^5 \text{ K s}^{-1}$ for the ACN-milled and untreated Al samples, respectively. Third, the cloud of burning Al particles and JP-10 vapor causes the droplet to ignite as a whole, and during this stage the temperature rises more slowly than in the Al-ignition stage reaching a maximum value after approximately 20 ms to 30 ms. Fourth, the temperature begins to

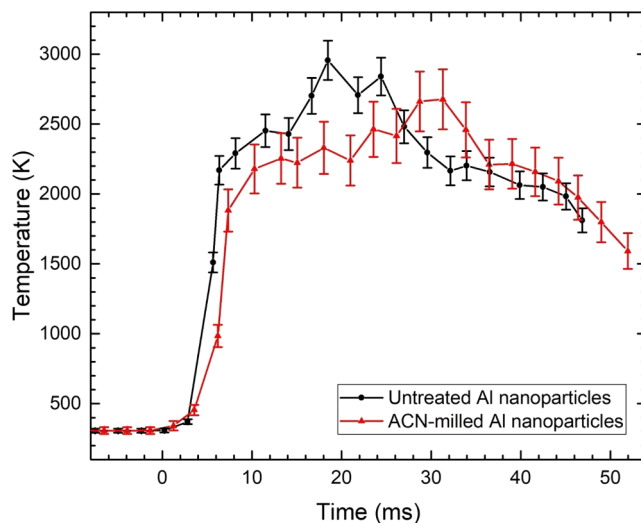


Fig. 1. Comparison between the temperature temporal profiles produced by igniting a JP-10 droplet containing untreated aluminum particles or acetonitrile-assisted ball-milled aluminum particles. The laser irradiation started at $t = 0$ s.

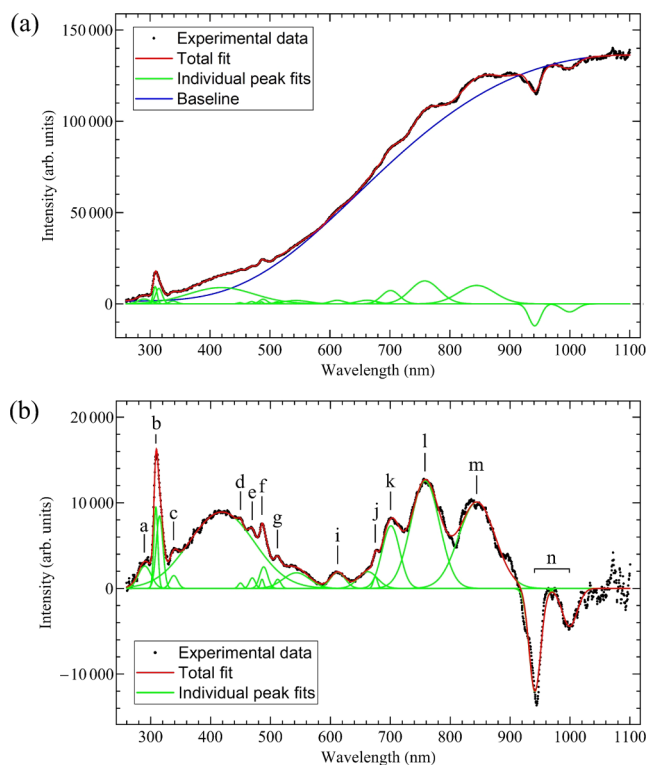


Fig. 2. (a) UV-Vis emission spectrum produced during ignition of a JP-10 droplet containing acetonitrile-assisted ball-milled aluminum particles. The total fit (red line) was obtained by simultaneously optimizing a black-body background (blue line) and 19 Gaussian peaks (green lines) across the 260 to 1100 nm wavelength range. (b) The same spectrum as shown in Fig. 2a except the black-body background has been subtracted to show the emission peaks and bands more clearly. The assignments of bands a-n are presented in Table 1. (For interpretation of the references to colour in this figure legend, the reader is referred to the web version of this article.)

decrease as the fuel was consumed. Finally, the hot surrounding gases [34] and the force from the ignition caused the droplet to fall out of the trap and onto the transducer below in a period approximately equal to the free fall time of 55 ms. The resulting splash ignited and, hence, produced a second ignition event together with an associated second temperature rise. To consider only combustion of the droplet, the data after the second temperature rise following approximately 50 ms are not shown or discussed further.

Although the temperature temporal profiles for the two types of nanoparticles have similar features overall, the two curves differ in some of their details. First, the maximum temperatures reached, T_{\max} , are higher for the untreated Al nanoparticles than for the ACN-milled Al nanoparticles:

$$T_{\max}(\text{untreated Al}) = 2930 \pm 120 \text{ K} \quad (2)$$

$$T_{\max}(\text{ACN-milled Al}) = 2610 \pm 170 \text{ K} \quad (3)$$

where the quoted values are the mean temperatures and standard deviations for five ignitions. To illustrate more realistically the stochastic nature of the combustion process, note that the temperature profiles in Fig. 1 are shown for a single ignition event rather than an average of several ignitions. Second, the Al ignition stage occurred more rapidly for the untreated Al nanoparticles, which resulted in an initial sharp temperature rise advanced by about 2 ms relative to the ACN-milled nanoparticles. Finally, the maximum temperature T_{\max} was reached earlier for the untreated Al, that is, after 18 ms rather than the 31 ms for the ACN-milled sample. Thus, the temporal profiles suggest that, although both types of nanoparticle enhance ignition of JP-10, the

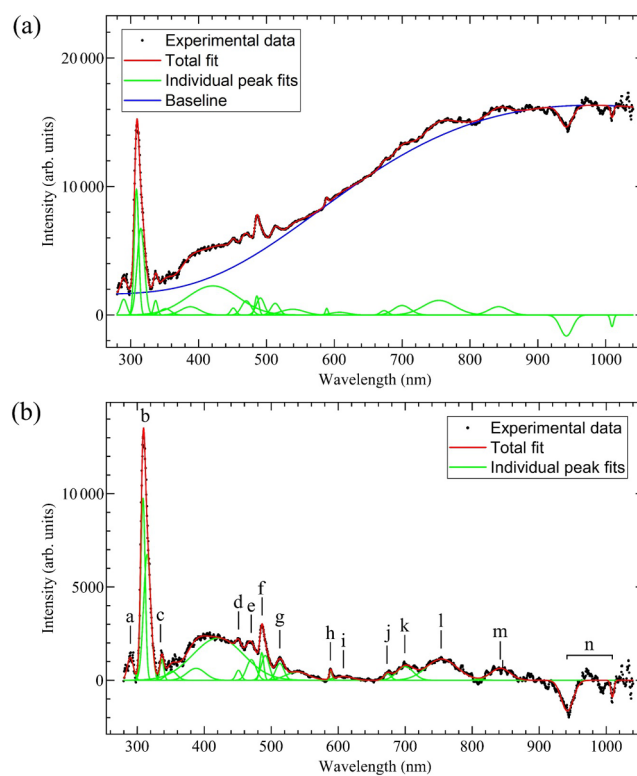


Fig. 3. (a) UV-Vis emission spectrum produced during ignition of a JP-10 droplet containing untreated Al particles. The total fit (red line) was obtained by simultaneously optimizing a black-body background (blue line) and 20 Gaussian peaks (green lines). (b) The same spectrum as shown in Fig. 3a except the black-body background has been subtracted. The assignments of bands a – n are presented in Table 1. (For interpretation of the references to colour in this figure legend, the reader is referred to the web version of this article.)

untreated Al nanoparticles produce initial temperature rises advanced by a few ms and higher maximum temperatures.

3.2. UV-visible emission spectroscopy

The UV-Vis emission spectra produced during ignition of a JP-10 droplet containing ACN-milled Al nanoparticles or untreated Al nanoparticles are shown in Figs. 2 and 3, respectively. The fits displayed in Fig. 2a and Fig. 3a were obtained by optimizing 19 or 20 Gaussian functions simultaneously with black-body functions to represent the backgrounds. The fitted Gaussians provided the wavelengths of the emission bands or peaks, whereas the optimized black-body functions enabled the flame temperatures to be deduced and gave $2690 \pm 50 \text{ K}$ and $2960 \pm 70 \text{ K}$ for the ACN-milled Al nanoparticles and untreated Al nanoparticles, respectively. In Fig. 2b and Fig. 3b, the same data are displayed but with the black-body backgrounds subtracted to illustrate the emission structures more clearly. The centers and vibrational mode assignments for bands (a) – (n) in the UV-Vis emission spectra are compiled in Table 1 and were discussed in detail in Ref. [30]. Briefly, the most prominent peak in the spectrum occurs at 310 nm, which is produced by an OH ($A^2\Sigma^+ - X^2\Pi$) transition. The four bands centered at 451 nm, 470 nm, 486 nm, and 513 nm are due to the $\Delta\nu = 2, 1, 0,$ and -1 transitions of aluminum monoxide (AlO) ($A^2\Sigma^+ - X^2\Sigma^+$), respectively, where $\Delta\nu$ denotes the change in the vibrational quantum number ν . The broad rise and decrease between around 300 nm and 500 nm is probably caused by unresolved emissions from the OH, C_2 , and CH radicals, which are known to dominate the UV-Vis spectra of hydrocarbon flames [35]. The very broad bands between approximately 600 nm and 900 nm are due to emissions from highly-excited vibrational states of water molecules which are prominent in this wavelength

Table 1

Vibrational mode assignments for the peaks or bands in the UV-Vis emission spectrum produced by igniting a JP-10 droplet containing untreated Al particles or acetonitrile-assisted ball-milled aluminum particles.

Peak or band	Peak wavelength or band center (nm) ^a	Peak wavelength or band center (nm) ^a	Molecule, atom, or radical	Ref. wavelength (nm)	Transition	Branch; vibrational quantum numbers: (ν' , ν'') or (ν_1', ν_2', ν_3') - ($\nu_1'', \nu_2'', \nu_3''$)
	ACN milled	Untreated				
a	290.1	289.7	OH	287.5–289.3 ^b	$A^2\Sigma^+ - X^2\Pi$	R ₁ , R ₂ , Q ₁ , Q ₂ ; (2, 1)
b	308.5	308.6	OH	309.0 ^b	$A^2\Sigma^+ - X^2\Pi$	Q ₂ ; (0, 0)
c	338.5	336.7	O ₂	337.0 ^b	$B^3\Sigma_u^- - X^3\Sigma_g^-$	(0, 14)
			HCO	337.6 ^b	A ₁	
d	449.9	451.1	AlO	453.8 ^b	$A^2\Sigma^+ - X^2\Sigma^+$	(5, 3)
e	469.6	470.3	AlO	467.2 ^b	$A^2\Sigma^+ - X^2\Sigma^+$	(2, 1)
			AlO	469.5 ^b	$A^2\Sigma^+ - X^2\Sigma^+$	(3, 2)
			C ₂	469.8 ^b	$A^3\Pi_g - X^3\Pi_u$	(3, 2)
f	485.9	485.9	AlO	484.2 ^b	$A^2\Sigma^+ - X^2\Sigma^+$	(0, 0)
			AlO	486.6 ^b	$A^2\Sigma^+ - X^2\Sigma^+$	(1, 1)
g	512.1	512.9	AlO	507.9 ^b	$A^2\Sigma^+ - X^2\Sigma^+$	(0, 1)
			AlO	510.2 ^b	$A^2\Sigma^+ - X^2\Sigma^+$	(1, 2)
			AlO	512.3 ^b	$A^2\Sigma^+ - X^2\Sigma^+$	(2, 3)
			C ₂	512.9 ^b	$A^3\Pi_g - X^3\Pi_u$	(1, 1)
h		588.9	Na	589.59 ^c	$^2S_{1/2} - ^2P_{3/2}$	(0, 0)
				589.00 ^c	$^2S_{1/2} - ^2P_{1/2}$	(1, 1)
i	612.3 (v. broad)	607.9	C ₂	612.2 ^b	$A^3\Pi_g - X^3\Pi_u$	(1, 3)
j	675.2	673.5				
k	701.1	699.7	H ₂ O	690–710 ^d	ro-vib. mode	(1, 0, 3)–(0, 0, 0)
l	758.2 (v. broad)	754.4	H ₂ O	712–737 ^d	ro-vib. mode	(3, 0, 1)–(0, 0, 0)
m	844.7 (v. broad)	842.2	H ₂ O	811–839 ^d	ro-vib. mode	(2, 1, 1)–(0, 0, 0)
n	941.4 999.6	942.0	H ₂ O	928–966 ^d	ro-vib. mode	(2, 0, 1)–(0, 0, 0)

^a Measurements are accurate to within 1 nm.

^b Ref. [35].

^c Ref. [38].

^d Ref. [36].

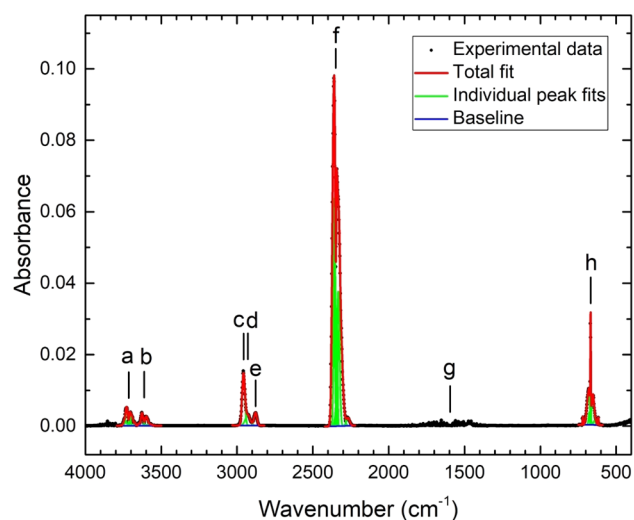


Fig. 4. FTIR transmission spectrum following ignition of a JP-10 droplet containing acetonitrile-assisted ball-milled aluminum nanoparticles. The rovibrational bands of the products and unreacted JP-10 are labelled (a)–(h) and assigned in Table 2. The total fit (red line) and individual peak fits peaks (green lines) are shown. (For interpretation of the references to colour in this figure legend, the reader is referred to the web version of this article.)

region [36]. The broad absorption region from approximately 900 nm to 1000 nm (or 11,110 to 10,000 cm^{-1}) could be because of the water vapor produced in the combustion (Table 1); however, absorption from the optical fiber in this range complicates simple interpretation. The emission lines in the UV-Vis spectra are produced by chemiluminescence, in which radicals are produced in electronically excited states via chemical reactions. The chemical reactions forming the excited states in Table 1 together with the energetics have been discussed in Ref. [30].

The data analysis above reveals that the UV-Vis emission spectra for the ACN-milled Al sample and the untreated Al sample can be interpreted in terms of the same atoms, molecules, and radicals; however, the relative amplitudes of the bands differ significantly. In particular, in the 300 nm to 520 nm wavelength range, the intensities of the OH and AlO emissions relative to the black-body background are significantly larger for the untreated Al sample (cf. Fig. 2a and Fig. 3a). The area of the structure produced by the unresolved (0,0) and (1,1) transitions of AlO ($A^2\Sigma^+ - X^2\Sigma^+$) at 486 nm and 489 nm, respectively, when normalized relative to the black-body background, is a factor of approximately three higher for the untreated Al nanoparticles. The increased amplitude of the AlO peaks is especially pertinent, since we established previously that the initiation and enhancement of the combustion of JP-10 droplets by the Al nanoparticles was because of the highly reactive aluminum monoxide (AlO) and atomic oxygen (O) formed when Al atoms reacted with molecular oxygen in the gas phase [30]. Therefore, the higher production of the AlO radicals for the untreated Al sample is consistent with the temperature temporal profiles presented in Section

Table 2

Vibrational mode assignments for bands (a) - (h) in the FTIR transmission spectrum produced following ignition of JP-10 droplets containing acetonitrile-assisted ball-milled aluminum particles.

Band	Centre wavenumber ^{a)} (cm ⁻¹)	Molecule	Ref. band centre (cm ⁻¹)	Number (symmetry)	Vibrational mode ^{b)}
a	3714	CO ₂	3714.8 ^{c)}	1(σ _g ⁺) + 3(σ _u ⁺)	combination band
b	3612	CO ₂	3612.8 ^{c)}	1(σ _g ⁺) + 3(σ _u ⁺)	combination band
c	2957	C ₁₀ H ₁₆	2942 ^{d)}	68	ν(CH)
d	2929	C ₁₀ H ₁₆	2913 ^{d)}	62	ν(CH ₂)
e	2878	C ₁₀ H ₁₆	2865 ^{d)}	57	ν(CH)
f	2349	CO ₂	2349.1 ^{e)}	3(σ _u ⁺)	ν _{as} (CO ₂)
g	≈ 1600	H ₂ O	1595 ^{e)}	2(a ₁)	δ(OH)
h	668	CO ₂	667.4 ^{e)}	2(π _u)	δ(CO ₂)

a) Uncertainties less than 1 cm⁻¹.

b) ν denotes stretch; δ, bend; and as, antisymmetric.

c) Ref. [37].

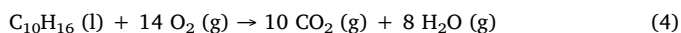
d) Ref. [39].

e) Ref. [38].

3.1, which showed that the untreated Al nanoparticles produced initial temperature rises advanced by a few ms and higher maximum temperatures.

3.3. FTIR spectroscopy

The FTIR transmission spectrum following ignition of a JP-10 droplet containing ACN-milled Al nanoparticles is shown in Fig. 4. The spectrum was collected along the full path length of the process chamber after the JP-10 had completely combusted. The bands of the products and evaporated JP-10 are labelled a) to h) in Fig. 4 and assigned in Table 2 to the vibrational modes of CO₂ [37], H₂O [38], and unreacted gas-phase JP-10 [39]. The water and carbon dioxide were formed by oxidation of JP-10:



Thus, FTIR transmission spectroscopy reveals only the standard products of hydrocarbon oxidation, namely, CO₂ and H₂O (reaction (4)). There was no evidence for the H₂, CH₄, C₂H₄, C₂H₆, or propene (C₃H₆) that desorbed from the ACN-milled Al nanoparticles during heating and were observed in the TGA-MS measurements [28]. Furthermore, we could not detect any nitrogen-containing final state molecules such as nitrogen dioxide (NO₂) or nitrous oxide (N₂O). Considering that 99% of the droplet (by wt.) was JP-10 and that the AlN_nC_mO_vH_x layer surrounding the ~34 nm diameter Al particles had a thickness of only 3.5 nm, the inability to detect molecules from the surface layer is not surprising.

The ATR-FTIR spectrum of the ACN-milled Al nanoparticles is shown in Fig. S1 of the Supporting Information. The spectrum consists of a smooth continuum only and there is no evidence for any discrete peaks produced by the vibrational modes of molecules. The broad background is mainly a consequence of the Al particles scattering the infrared beam out of the path of the ATR accessory. Similarly, the Raman spectrum of the ACN-milled Al nanoparticles, as shown in Fig. S2 of the Supporting Information, is a smooth structureless continuum. The absence of discrete peaks in the Raman spectrum is a general characteristic of amorphous surface layers which lack crystalline order. Yu et al (2016) likewise could not detect any vibrational modes in their diffuse reflectance and ATR-FTIR measurements of the ACN-milled Al nanoparticles [28].

4. Conclusion

We used the levitator experimental set-up to investigate the effects of ACN-milled Al nanoparticles on the ignition of JP-10 droplets acoustically levitated in an oxygen-argon mixture. The results were

compared with those for standard 100 nm-diameter untreated Al particles, which are surrounded by an amorphous Al₂O₃ layer. A carbon dioxide laser was used to ignite the Al-containing JP-10 droplets, and the induced combustion processes were followed via UV-Vis, FTIR, and Raman spectroscopies together with high-speed optical and infrared thermal-imaging cameras.

The temperature temporal profiles for the two types of Al nanoparticles had similar overall shapes but differed in some key respects. First, the initial sharp temperature rise during the Al-ignition stage occurred about 2 ms earlier for the untreated Al particles relative to the ACN-milled Al particles. Second, the maximum temperature reached, T_{max}, was higher for the untreated Al sample than for the ACN-milled Al sample, that is, 2930 ± 120 K and 2610 ± 170 K, respectively. Finally, these maximum temperatures were attained sooner for the untreated Al particles. In the 300 nm to 520 nm wavelength range of the UV-Vis emission spectra, the intensities of the OH and AlO bands were significantly larger for the untreated Al samples. In our previous study, we suggested that the initiation and enhancement of the combustion of Al-containing JP-10 droplets are a consequence of forming highly-reactive AlO radicals when Al atoms reacted with molecular oxygen in the gas phase [30]. Therefore, the increased production of AlO radicals for the untreated Al sample is consistent with the temperature temporal profiles, which showed that the untreated Al nanoparticles enhanced ignition more than the ACN-milled nanoparticles. Thus, the present measurements suggest that the AlN_nC_mO_vH_x surface layer on the ACN-milled Al nanoparticles, perhaps as a consequence of forming strong Al-N bonds, limits oxidation of the Al core to a greater extent than the amorphous Al₂O₃ surface layer surrounding standard Al nanoparticles. We note that the smaller diameter of the ACN-milled Al nanoparticles does not alter this conclusion, since reducing the diameter of Al particles increases the combustion rate [19–23]. Alternatively, the flat, plate-like structures produced by the milling reduce the mass of the unoxidized Al core relative to the passivating Al₂O₃ surface layer. The resulting reduction in the Al available for oxidation could explain why the ACN-milled sample enhances the ignition less than the untreated Al nanoparticles. The other effect of the plate-like shape is to increase the surface-area-to-volume ratio; however, this would increase the absorption of heat from the CO₂ laser and, therefore, cannot explain the reduced enhancement. A reduced ignition delay time or a higher maximum temperature increases the pressure produced by gas-phase jet fuel [40] and ultimately, therefore, the thrust available from a jet propulsion system. The slight increase in the ignition delay times and the reduced maximum temperatures for the ACN-milled nanoparticles would consequently be a minor disadvantage for application in hydrocarbon fuels.

Declaration of Competing Interest

The authors declare that they have no known competing financial interests or personal relationships that could have appeared to influence the work reported in this paper.

Acknowledgement

This work was supported by the Office of Naval Research under contract number N000141912083.

Appendix A. Supplementary material

Supplementary data to this article can be found online at <https://doi.org/10.1016/j.cplett.2020.137679>.

References

- [1] H.S. Chung, C.S.H. Chen, R.A. Kremer, J.R. Boulton, G.W. Burdette, Recent developments in high-energy density liquid hydrocarbon fuels, *Energy Fuels* 13 (1999) 641–649.
- [2] M.B. Colket, L.J. Spadaccini, Scramjet fuels autoignition study, *J. Propul. Power* 17 (2001) 315–323.
- [3] T.J. Bruno, M.L. Huber, A.D. Laesecke, E.W. Lemmon, R.A. Perkins, Thermochemical and thermophysical properties of JP-10, NIST Interagency/Internal Report (NISTIR) 1–66 (2006), <https://doi.org/10.6028/NIST.IR.6640>.
- [4] A. Osmont, I. Gokalp, L. Catoire, Evaluating missile fuels, *Propellants Explos. Pyrotech.* 31 (2006) 343–354.
- [5] L. Zhao, T. Yang, R.I. Kaiser, T.P. Troy, B. Xu, M. Ahmed, J. Alarcon, D. Belisario-Lara, A.M. Mebel, Y. Zhang, C.C. Cao, J.B. Zou, A vacuum ultraviolet photo-ionization study on high-temperature decomposition of JP-10 (exo-tetrahydrodicyclopentadiene), *PCCP* 19 (2017) 15780–15807.
- [6] J.D. Cox, D.D. Wagman, V.A. Medvedev, CODATA key values for thermodynamics, Hemisphere Pub. Corp, New York, 1989.
- [7] S.C. Wong, S.R. Turns, Ignition of aluminum slurry droplets, *Combust. Sci. Technol.* 52 (1987) 221–242.
- [8] S.R. Turns, S.C. Wong, E. Ryba, Combustion of aluminum-based slurry agglomerates, *Combust. Sci. Technol.* 54 (1987) 299–318.
- [9] S.C. Wong, A.C. Lin, Microexplosion mechanisms of aluminum carbon slurry droplets, *Combust. Flame* 89 (1992) 64–76.
- [10] C. Allen, G. Mittal, C.J. Sung, E. Toulson, T. Lee, An aerosol rapid compression machine for studying energetic-nanoparticle-enhanced combustion of liquid fuels, *Proc. Combust. Inst.* 33 (2011) 3367–3374.
- [11] I. Javed, S.W. Baek, K. Waheed, Autoignition and combustion characteristics of heptane droplets with the addition of aluminium nanoparticles at elevated temperatures, *Combust. Flame* 162 (2015) 191–206.
- [12] V.V. Smirnov, S.A. Kostitsa, V.D. Kobtsev, N.S. Titova, A.M. Starik, Experimental study of combustion of composite fuel comprising n-decane and aluminum nanoparticles, *Combust. Flame* 162 (2015) 3554–3561.
- [13] E. Xiu-tian-feng, L. Pan, F. Wang, L. Wang, X.W. Zhang, J.J. Zou, Al-nanoparticle-containing nanofluid fuel: Synthesis, stability, properties, and propulsion performance, *Ind. Eng. Chem. Res.* 55 (2016) 2738–2745.
- [14] L.J. Liu, Q. Zhang, S.L. Shen, D. Li, Z. Lian, Y.X. Wang, Evaluation of detonation characteristics of aluminum/JP-10/air mixtures at stoichiometric concentrations, *Fuel* 169 (2016) 41–49.
- [15] Y. Luo, X. Xu, J.J. Zou, X.W. Zhang, Combustion of JP-10-based slurry with nanosized aluminum additives, *J. Propul. Power* 32 (2016) 1167–1177.
- [16] E. Xiu-tian-feng, L. Zhang, F. Wang, X.W. Zhang, J.J. Zou, Synthesis of aluminum nanoparticles as additive to enhance ignition and combustion of high energy density fuels, *Front. Chem. Sci. Eng.* 12 (2018) 358–366.
- [17] J.Z. Liu, B.H. Chen, T.T. Wu, W.J. Yang, J.H. Zhou, Ignition and combustion characteristics and agglomerate evolution mechanism of aluminum in nAl/JP-10 nanofluid fuel, *J. Therm. Anal. Calorim.* 137 (2019) 1369–1379.
- [18] B.H. Chen, J.Z. Liu, H.P. Li, W.J. Yang, K.F. Cen, Laser ignition and combustion characteristics of Al/JP-10 nanofluid droplet, *J. Therm. Anal. Calorim.* 135 (2019) 925–934.
- [19] J.J. Granier, M.L. Pantoya, Laser ignition of nanocomposite thermites, *Combust. Flame* 138 (2004) 373–383.
- [20] R.A. Yetter, G.A. Risha, S.F. Son, Metal particle combustion and nanotechnology, *Proc. Combust. Inst.* 32 (2009) 1819–1838.
- [21] E.L. Dreizin, Metal-based reactive nanomaterials, *Prog. Energy Combust. Sci.* 35 (2009) 141–167.
- [22] Y. Huang, G.A. Risha, V. Yang, R.A. Yetter, Effect of particle size on combustion of aluminum particle dust in air, *Combust. Flame* 156 (2009) 5–13.
- [23] D.S. Sundaram, V. Yang, V.E. Zarko, Combustion of nano aluminum particles (Review), *Combust. Explosion Shock Waves* 51 (2015) 173–196.
- [24] J.P.L. Perez, J. Yu, A.J. Sheppard, S.D. Chambreau, G.L. Vaghjiani, S.L. Anderson, Binding of alkenes and ionic liquids to B-H-functionalized boron nanoparticles: Creation of particles with controlled dispersibility and minimal surface oxidation, *ACS Appl. Mater. Interf.* 7 (2015) 9991–10003.
- [25] S.W. Chung, E.A. Gulians, C.E. Bunker, D.W. Hammerstroem, Y. Deng, M.A. Burgers, P.A. Jelliss, S.W. Buckner, Capping and passivation of aluminum nanoparticles using alkyl-substituted epoxides, *Langmuir* 25 (2009) 8883–8887.
- [26] K.A.S. Fernando, M.J. Smith, B.A. Harruff, W.K. Lewis, E.A. Gulians, C.E. Bunker, Sonochemically assisted thermal decomposition of alane N, N-dimethylethylamine with titanium (IV) isopropoxide in the presence of oleic acid to yield air-stable and size-selective aluminum core-shell nanoparticles, *J. Phys. Chem. C* 113 (2009) 500–503.
- [27] M.J. Meziani, C.E. Bunker, F.S. Lu, H.T. Li, W. Wang, E.A. Gulians, R.A. Quinn, Y.P. Sun, Formation and properties of stabilized aluminum nanoparticles, *ACS Appl. Mater. Interf.* 1 (2009) 703–709.
- [28] J. Yu, B.W. McMahon, J.A. Boatz, S.L. Anderson, Aluminum nanoparticle production by acetonitrile-assisted milling: Effects of liquid- vs vapor-phase milling and of milling method on particle size and surface chemistry, *J. Phys. Chem. C* 120 (2016) 19613–19629.
- [29] V.I. Levitas, M.L. Pantoya, S. Dean, Melt dispersion mechanism for fast reaction of aluminum nano- and micron-scale particles: Flame propagation and SEM studies, *Combust. Flame* 161 (2014) 1668–1677.
- [30] M. Lucas, S.J. Brotton, A. Min, C. Woodruff, M.L. Pantoya, R.I. Kaiser, Effects of size and prestressing of aluminum particles on the oxidation of levitated exo-tetrahydrodicyclopentadiene droplets, *J. Phys. Chem. A* 124 (2020) 1489–1507.
- [31] S.J. Brotton, R.I. Kaiser, Novel high-temperature and pressure-compatible ultrasonic levitator apparatus coupled to Raman and Fourier transform infrared spectrometers, *Rev. Sci. Instrum.* 84 (2013) 055114.
- [32] S.J. Brotton, M. Lucas, T.N. Jensen, S.L. Anderson, R.I. Kaiser, Spectroscopic study on the intermediates and reaction rates in the oxidation of levitated droplets of energetic ionic liquids by nitrogen dioxide, *J. Phys. Chem. A* 122 (2018) 7351–7377.
- [33] D. Drysdale, An introduction to fire dynamics, third ed., Wiley, Chichester, West Sussex, 2011.
- [34] C.P. Lee, T.G. Wang, Acoustic radiation force on a heated sphere including effects of heat-transfer and acoustic streaming, *J. Acoust. Soc. Am.* 83 (1988) 1324–1331.
- [35] A.G. Gaydon, The spectroscopy of flames, second ed., Chapman and Hall; Halsted Press Division, London, New York, 1974.
- [36] I.E. Gordon, L.S. Rothman, C. Hill, R.V. Kochanov, Y. Tan, et al., The HITRAN2016 molecular spectroscopic database, *J. Quant. Spectrosc. Radiat. Transfer* 203 (2017) 3–69.
- [37] C.E. Miller, L.R. Brown, Near infrared spectroscopy of carbon dioxide I. $^{16}\text{O}^{12}\text{C}^{16}\text{O}$ line positions, *J. Mol. Spectrosc.* 228 (2004) 329–354.
- [38] P.J. Linstrom and W.G. Mallard, Eds., NIST Chemistry WebBook, NIST Standard Reference Database Number 69, National Institute of Standards and Technology, Gaithersburg MD, 20899, <https://doi.org/10.18434/T4D303>, (retrieved May 7, 2020).
- [39] M. Lucas, S.J. Brotton, A. Min, M.L. Pantoya, R.I. Kaiser, Oxidation of levitated exo-tetrahydrodicyclopentadiene droplets doped with aluminum nanoparticles, *J. Phys. Chem. Lett.* 10 (2019) 5756–5763.
- [40] S.S. Vasu, D.E. Davidson, R.K. Hanson, Jet fuel ignition delay times: Shock tube experiments over wide conditions and surrogate model predictions, *Combust. Flame* 152 (2008) 125–143.